Experimental Methods and Characterization Techniques

2. Experimental

This chapter comprises the specifications of the chemicals used during the experimentations. All the experimental procedures, synthesis methodologies, physico-chemical and electrochemical characterization techniques implemented during the study are comprehensively elaborated in this section.

2.1. Materials and Reagents

The chemicals and reagents used throughout the experiments are summarized in Table 2.1. All the chemicals were used as received without further purification. The experiments were carried out using distilled water.

Table 2.1. List of Chemicals*

Chemicals	Purchased from
Cobalt(II) chloride hexahydrate ($CoCl_2 \cdot 6H_2O$, 99.0%), Iron(III) chloride hexahydrate ($FeCl_3 \cdot 6H_2O$, ≥99%), Manganese(II) chloride tetrahydrate ($MnCl_2 \cdot 4H_2O$, ≥99%), Ammonium cerium(IV) nitrate [$(NH_4)_2Ce(NO_3)_6$, ≥98.5%], Ethanol (C_2H_5OH, ACS, ISO, Reag., ≥99.5%), Potassium hydroxide (KOH, ≥84.0%), Sodium hydroxide (NaOH, 99.0%), 2-Propanol [$(CH_3)_2CHOH$, ≥99.5 %], glucose ($C_6H_{12}O_6$, ≥99.5%), ethylene glycol ($C_2H_6O_2$, anhydrous, 99.8%), urea (CH_4N_2O, reagent grade, 98%) and hydrochloric acid (HCl, EMSURE® ACS, ISO, Reag. Ph Eur).	Merck
Nafion, 20 wt.% Pd/C, RuO_2 20 wt.% Pt/C	Alfa Aesar Johnson Matthey and Alfa Aesar
Vulcan XC-72R carbon (VC)	Cabot Corporation, as gift

*All the chemicals were used as such without any further purification.

2.2. Synthesis of Nano-Electrocatalysts

The as-synthesized nano-ECs were mainly synthesized via hydrothermal and solvothermal methods.

2.2.1. Synthesis of Co_3O_4/C

In a typical procedure, 0.1 mol of $CoCl_2 \cdot 6H_2O$ was continuously stirred in 40 mL of H_2O using a magnetic stirrer for 30 min followed by a gentle and dropwise addition of 40 mL 0.5 M NaOH solution. The obtained pink turbid suspension was magnetically stirred for 1 h before being transferred to a Teflon-lined stainless-steel autoclave and then heated in an electric oven at 180 °C for 6 h. A pink product was harvested after centrifugation and dried at 60 °C for 12 h. Finally, the product was calcined at 450 °C for 4 h in an air atmosphere. The Co_3O_4/C are prepared by blending the as-synthesized Co_3O_4 and VC (3:7 wt. ratio) followed by ultrasonication in C_2H_5OH. Finally, the products were dried at 60 °C for 12 h.

2.2.2. Synthesis of Carbon-Supported Co_3O_4 Nanooctahedron (Oct-Co_3O_4/C)

In a typical process 0.1 mol of $CoCl_2 \cdot 6H_2O$ was continuously stirred in 40 mL of 1:1 H_2O/C_2H_5OH using a magnetic stirrer for 30 min followed by a gentle and dropwise addition of 40 mL 0.5 M NaOH solution. The reaction mixture was allowed to stand for 1 h with constant stirring and trasferred to a Teflon-lined stainless-steel autoclave. To obtain shape-controlled nanooctahedron morphology of Co_3O_4, the reaction temperature was optimized at 120 °C for 6 h. After the autoclave was cooled to room temperature, the resulting precipitate was separated by centrifugation, washed with distilled water and C_2H_5OH several times, and dried in an oven at 60 °C for 12 h. The dried product was then calcinated in a muffle furnace at 300 °C for 3 h in an air atmosphere. The 30 wt.% Oct-Co_3O_4/C was prepared by following the same method as discussed in 2.2.1. The schematic of the synthesis strategy of Oct-Co_3O_4/C is demonstrated in Scheme 2.2.1.

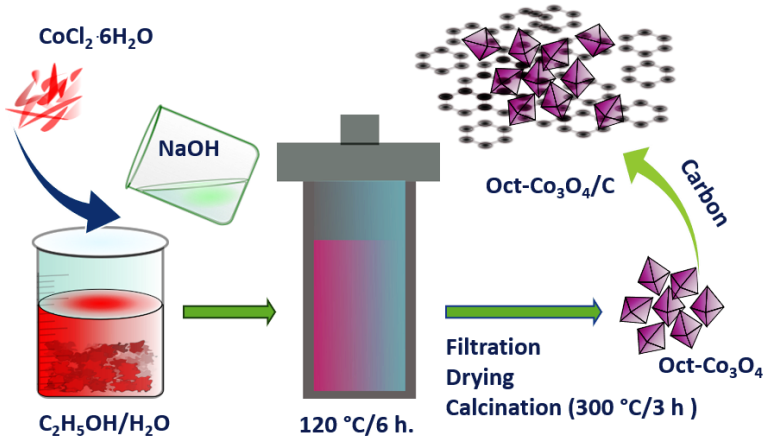

Scheme 2.2.1: Schematic illustration of the synthesis of Oct-Co_3O_4/C.

2.2.3. Synthesis of Carbon-Supported Sponge-like Co_3O_4 (Sp-Co_3O_4/C)

To synthesize morphology-controlled cobalt oxide, 9.5172 g of $CoCl_2 \cdot 6H_2O$ and 7.2062 g of glucose were first dissolved in 40 mL of 1:1 ethylene glycol: distilled water solution at room temperature, followed by the addition of 0.2402 g of urea solution (40 mL of 1:1 ethylene glycol/distilled water solution) while stirring.

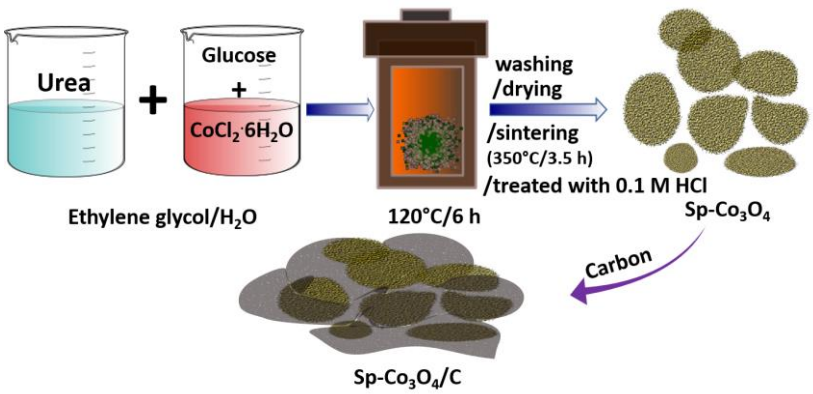

Scheme 2.2.2: Schematic illustration of the synthesis of Sp-Co_3O_4/C.

Then the mixture was transferred to a Teflon-lined stainless-steel autoclave and kept inside the electric oven at 120 °C for 6 h. After the autoclave was cooled to room temperature, the resulting precipitate was separated by centrifugation, washed with distilled water and C_2H_5OH several times, and dried in the oven at 80 °C for 12 h. The dried product was then sintered at 350 °C for 3.5 h. The resultant product was treated with 0.1 M hydrochloric acid (HCl). The 30 wt.% Sp-Co_3O_4/C was prepared

by following the same method as discussed in 2.2.1. The steps involved in the synthesis process are schematically shown in Scheme 2.2.2.

2.2.4. Synthesis of α-MnO_2/Mn_3O_4/CeO_2/C hybrid

The synthesis of the α-MnO_2/Mn_3O_4/CeO_2 hybrid was performed via solvothermal reaction in a Teflon-lined stainless-steel autoclave followed by calcination. NaOH (1.6 g, 1 M, 40 mL) was added to a solution of $MnCl_2{\cdot}4H_2O$ (0.32 g, 0.05 M) and $(NH_4)_2Ce(NO_3)_6$ (1.1 g, 0.05 M) prepared in a 40 mL 1:1 water (distilled water) / C_2H_5OH solvent system. The mixture was allowed to stand for 30 min with constant stirring at room temperature. The resulting solution was trasferred to a Teflon-lined stainless-steel autoclave and held at 120 °C for 6 h. The final product obtained was then centrifuged and thoroughly washed 6-8 times with distilled water and three times with 1:1 C_2H_5OH /water mixture. The resulting product was dried at 60 °C for 12 h. The oxide catalyst precursor was obtained by calcination of the precursor in a muffle furnace at 450 °C for 4 h. The 30 wt.% α-MnO_2/Mn_3O_4/CeO_2/C was prepared by following the same method as discussed in 2.2.1. The steps involved in the synthesis process are schematically shown in Scheme 2.2.3.

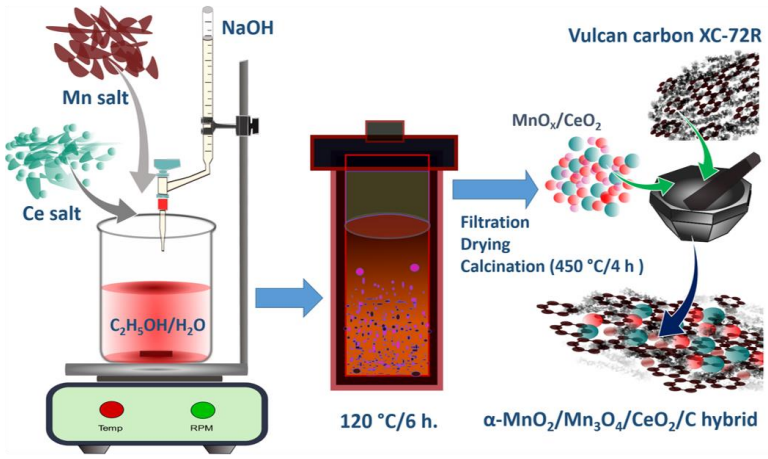

Scheme 2.2.3: Schematic illustration of the synthesis of α-MnO_2/Mn_3O_4/CeO_2/C hybrid.

2.2.5. Synthesis of α-MnO_2/Mn_3O_4/C

α-MnO_2/Mn_3O_4 were synthesized following the same solvothermal method as mentioned in section 2.2.2. NaOH (1.6 g, 1 M, 40 mL) was added to a solution of $MnCl_2{\cdot}4H_2O$ (0.65 g, 0.1M) prepared in a 40 mL 1:1 water (distilled) / C_2H_5OH solvent system. The mixture was allowed to stand for 30 min with constant stirring at room temperature. The resulting solution was transferred to a Teflon-lined stainless-steel autoclave and held at 120 °C for 6 h. The final product obtained was then centrifuged and thoroughly washed 6-8 times with distilled water and three times with 1:1 C_2H_5OH /water mixture. The resulting product was dried at 60 °C for 12 h. The oxide catalyst precursor was obtained by calcination of the precursor in a muffle furnace at 450 °C for 4 h. The 30 wt.% α-MnO_2/Mn_3O_4/C was prepared by following the same method as discussed in 2.2.1.

2.2.6. Synthesis of α-MnO_2/Mn_3O_4/CeO_2/C-37 and α-MnO_2/Mn_3O_4/CeO_2/C-73

These syntheses were made to vary the CeO_2 content in α-MnO_2/Mn_3O_4/CeO_2/C. The molar concentration of the precursor salt $MnCl_2{\cdot}4H_2O$ and $(NH_4)_2Ce(NO_3)_6$ were modified as 3:7 and 7:3, respectively for the synthesis of α-MnO_2/Mn_3O_4/CeO_2/C-37, α-MnO_2/Mn_3O_4/CeO_2/C-73. All other experimental conditions are the same as discussed in section 2.2.4.

2.2.7. Synthesis of Fe_2O_3-CeO_2/C

Fe_2O_3-CeO_2/C was also synthesized in a similar method as discussed in section 2.2.4. using $FeCl_3{\cdot}6H_2O$ (0.54 g, 0.05 M) as precursor salt, keeping all other experimental conditions unaltered.

2.2.8. Synthesis of Fe_2O_3/C

Fe_2O_3 was synthesized following the same solvothermal method as mentioned in section 2.2.4. In this procedure, a single metal salt *i.e.*, $FeCl_3{\cdot}6H_2O$ (1.08 g, 0.1 M) was used as precursor salt and all other experimental conditions were kept unaltered.

2.2.9. Synthesis of Fe_2O_3-CeO_2/C-37 and Fe_2O_3-CeO_2/C-73

Fe_2O_3-CeO_2/C-37 and Fe_2O_3-CeO_2/C-73 were synthesised to vary the CeO_2 content in Fe_2O_3-CeO_2/C as discussed in section 2.26. The molar concentration of the precursor salt $FeCl_3{\cdot}6H_2O$ and $(NH_4)_2Ce(NO_3)_6$ were modified as 3:7 and 7:3, respectively for the synthesis of Fe_2O_3-CeO_2/C-37 and Fe_2O_3-CeO_2/C-73. All other experimental conditions are the same as discussed in section 2.2.4.

2.2.10. Synthesis of CuO/C

CuO was synthesized employing the similar solvothermal method as mentioned in section 2.2.4. In this process, a single metal salt *i.e* $CuCl_2{\cdot}2H_2O$ (0.681 g, 0.1 M) was used as precursor salt and all other experimental conditions were kept unaltered.

2.2.11. Synthesis of CuO/CeO_2/C

CuO/CeO_2/C was also synthesized in a analogous method as discussed in section 2.2.4 using $CuCl_2{\cdot}2H_2O$ (0.34 g, 0.05 M) and $(NH_4)_2Ce(NO_3)_6$ (1.1 g, 0.05 M) as the precursor salt, keeping all other experimental conditions unaltered.

2.2.12. Synthesis of CeO_2/C

CeO_2/C was also synthesized in a similar method as discussed in section 2.2.5. However, a single metal salt *i.e.*, $(NH_4)_2Ce(NO_3)_6$ (2.19 g, 0.1 M) as the precursor salt was chosen, keeping all other experimental conditions unaltered.

2.3. Characterization Techniques

The as-prepared nanostructures were characterized by different analytical techniques to study the physical and chemical properties which are briefly described in the following sub-sections.

2.3.1. Scattering-Based Techniques for Material Characterization

2.3.1.1. Powder X-Ray Diffraction (XRD)

XRD is a very sophisticated and non-destructive technique that gives valuable insight into the structural parameters (such as cell dimension, crystallite size, bond

angles *etc*.) and phase (crystalline or amorphous) of the unit cell. The sample to be analyzed should be finely ground and homogeneous. This technique also gives information about the interplanar distance which is determined using Bragg's equation,

$$n\lambda = 2d \sin\theta \qquad (2.1)$$

where, 'd' is the lattice spacing, 'θ' is the angle of the X-ray beam concerning the lattice plane, 'λ' is the wavelength of the X-ray beam and 'n' is the order of lattice planes.

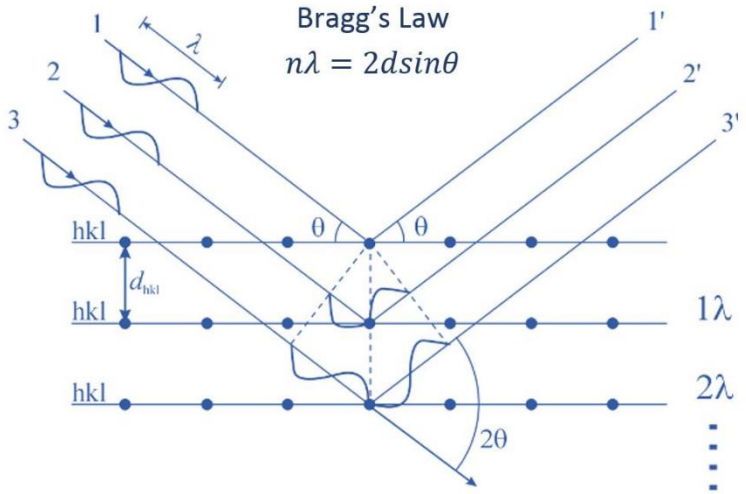

Figure 2.2.1. Schematic illustration of Bragg's Law.

The fundamental principle is based on the constructive interference which is produced during the interaction of the incident monochromatic rays with the sample and satisfies Bragg's law (Figure 2.2.1). The X-rays are produced by a cathode ray tube and get filtered to obtain monochromatic radiations [1,2]. The diffracted X-rays were detected at various angles, processed and then counted. The diffracted X-rays from the atomic layers of the specimen were detected, counted and investigated. All the possible diffraction patterns of the lattice are obtained due to the random orientation of the finely powdered materials. The conversion of the diffraction peaks to d-spacing allows the identification of the material because each material has a set of unique d-spacing, which could be achieved or identified by comparing it with the standards [2]. Besides, the peak position, intensity and width give the desired information about the materials. The reference diffraction patterns accessible from

the International Centre for Diffraction Data (ICDD, formerly acknowledged as Joint Committee on Powder Diffraction Standards, JCPDS) are used to compare the intensity and position of the peaks for confirmation [3,4]. The average crystallite size (D) can be determined using Scherrer's equation as follows:

$$D = K\lambda/\beta_{2\theta}\cos\theta \qquad (2.2)$$

Where, λ is the wavelength of the X-ray source, $\beta_{2\theta}$ is the full width at half maximum (FWHM), θ is the diffraction angle (radian), K is the shape factor, and L is the mean size of the ordered (crystalline) domain.

In the current study, the XRD patterns of all the synthesized materials were recorded on a Bruker AXS Model D8 focus instrument using a nickel-filtered CuK_α radiation source with $\lambda = 0.15418$ nm in the 2θ range of 10 – 80°. The corresponding scan rate was 0.05° s^{-1}.

2.3.1.2. Raman Scattering

Raman spectroscopy is a powerful scattering-based technique which is used to understand the vibrational modes, phase transitions as well as structural defects in nanostructures [5]. This non-destructive technique can also differentiate between ordered and disordered carbon present in carbon-supported nanomaterials. Generally, all carbon-containing samples exhibit two broad peaks around ~1350 and ~1580 cm^{-1}, known as D- and G-band, respectively. D-band corresponds to the disorders in the sp^3-hybridized carbon atom, while G-band to the vibration associated with sp^2 hybridized graphitic carbon atoms [6,7].

The basic principle of Raman spectroscopy is the assortment of scattered lights created after the interaction of a laser with a sample. Usually, the scattered light retains the equivalent frequency as the excitation source; which is termed Rayleigh scattering [8]. However, when the vibrational energy levels of the molecules in the sample interact with the excitation source a significant shift occurs in the scattered lights as shown in Figure 2.2.2. Thus, the plot of the intensity of the Raman scatters vs. frequency provides the signal about the vibrational modes generated due to the change in polarization of the sample in the actions of the electromagnetic waves [8].

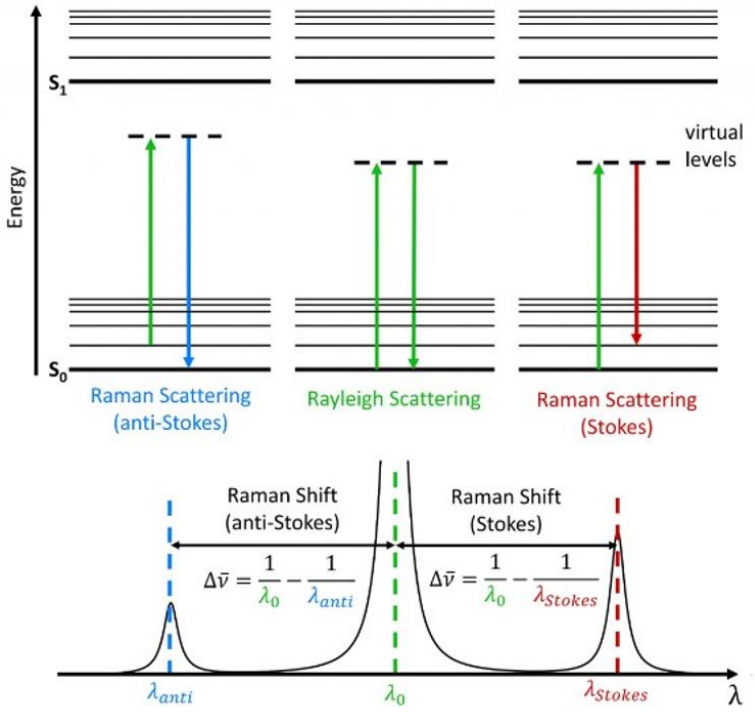

Figure 2.2.2. Jablonski Diagram showing the origin of different Raman scatterings. (Adapted from [9])

The chief advantages of Raman spectroscopy include easy handling of the instrument, low sample damage, high sensitivity and measurement of samples via light transparent materials [10]. In this study, Raman spectra of the carbon-supported samples were collected in a Renishaw, U.K. Raman spectrometer using a 514 nm laser (Ar^+ ion) as the excitation source with a laser power of 5 mW.

2.3.2. Electron Microscopy Based Techniques for Material Characterization

The techniques that will be covered under electron microscopy are mainly scanning electron microscopy (SEM) and transmission electron microscopy (TEM). These techniques utilize a beam of energetic electrons that are accelerated to produce a high-resolution image.

2.3.2.1. Scanning Electron Microscopy (SEM)

SEM is one of the efficient methods that help analyse both organic and inorganic materials in the range of nano- to micro-meter. SEM is typically based on

the interaction of a high-energy electron beam (100–30,000 eV) with the sample surface. Since a very narrow beam of electron is applied; SEM generally produces 3-D images which are useful to understand the surface morphology of the solid specimen. The signals obtained from the electron-sample interaction offer information about the surface morphology, the orientation of particles, crystallinity as well as chemical composition [4,11,12]. In the current study, SEM images were obtained using the "JEOL, JSM Model 6390 LV" scanning electron microscope, operating at an accelerating voltage of 15 kV.

2.3.2.2. Scanning Transmission Electron Microscopy (STEM)

STEM is a significant tool for the physical characterization of nanostructures. It offers elemental composition and crystal information at the atomic scale. The STEM works on the same principle as a normal scanning electron microscope by focusing an electron beam into a very small spot which is scanned over the TEM sample. The difference with SEM is that one has to prepare ultrathin specimens of 200 nm or less (except for nanoparticles) so that the accelerated beam of electrons passes through the sample. This electron beam interacts with the TEM sample and the transmitted beam is collected by a detector. This can either be a CCD chip (when operating in TEM mode) or a high angle annular dark field (HAADF) detector [4,11,12]. In this work, HAADF-STEM images of the investigated samples were recorded on a JEM-2100F, JEOL microscope operating at 200 kV.

2.3.2.3. Transmission Electron Microscopy (TEM) and High-Resolution Transmission Electron Microscopy (HRTEM)

TEM is the most commonly used technique for the determination of shape, size, distribution and homogeneity of the NPs with accuracy. TEM involves the interaction between electron beams (energy in the range of 60–120 keV) having uniform current density and the sample of a thin layer. Various factors such as elemental composition, size and morphology determine the magnitude of interaction. When the beam of electron falls on the sample, a part of it is transmitted, while the remaining are scattered elastically or inelastically. The desired image is obtained from the signals derived from the transmitted electrons [3]. The SAED pattern

obtained during analysis is used to determine the crystalline nature of the material and also the presence of interfaces and twin defects. HRTEM images provide information about the interplanar-spacing '*d*' in various associated planes. TEM and HRTEM images were obtained on a JEM-2100 instrument with an accelerating voltage of 200 kV in 50 V steps. Before imaging, the sample is dispersed in ethanol (solvent) via ultrasonication and the resultant ink is drop-casted on the carbon foil supported on the Cu grid [13].

2.3.3. X-Ray Based Techniques for Material Characterization

2.3.3.1. X-Ray Photoelectron Spectroscopy (XPS)

XPS is one of the extensively used and very powerful techniques for surface property analysis. XPS is useful for quantitative analysis of surface composition and can detect all elements except for H and He through the detection of the binding energies of the photoelectrons. It gives information about the elemental composition, the local atomic environment of the surface, oxidation states of the constituting elements and electronic structure [3,14].

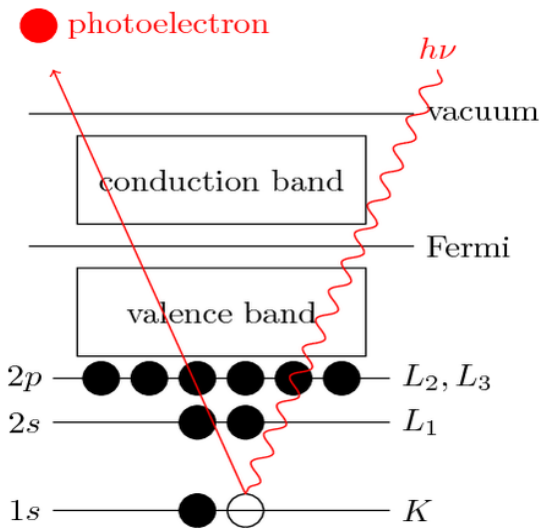

Figure 2.2.3. Schematic diagram of photoemission process used for XPS.

The basic principle of XPS is the photoelectric effect and functions under ultra-high vacuum which was discovered by Hertz in 1887 [15,16] and extended to surface analysis by K. Siegbahn and his research group at Uppsala University,

Sweden, during the mid-1960s. When a high energy beam (X-ray photon) is allowed to interact with the sample surface, the energy of the incident X-ray ($h\nu$) is absorbed by the core electron of an atom followed by ejected out from it. The ejected electron with a kinetic energy of E_k is termed a photoelectron. The schematic representation of the photoemission is shown in Figure 2.2.3. The binding energy (E_b) of the core electron is given by the Einstein relationship (Equation **2.3**.)[17]

$$h\nu = E_b + E_k + \Phi \qquad (2.3)$$

where, $h\nu$ is the X-ray photon energy (for Al Kα = 1486.6 eV, for Mg Kα = 1253.6 eV), E_k is the kinetic energy of the photoelectron; Φ is the work function of the spectrometer (4 ~5 eV) and E_b is the binding energy of the core electron.

In brief, the sample is irradiated with monochromatic x-rays, resulting in the emission of photoelectrons whose energies are characteristic of the elements within the sampling volume. An XPS spectrum is created by plotting the number of ejected electrons versus their binding energy. In the current work, XPS was conducted using a Shimadzu ESCA-3400 system with an Mg-anode X-ray gun (10 kV, 20 mA). Before measurements, all of the samples were Ar-etched for 60 s. During data processing, the binding energies (BEs) of all of the samples were calibrated against the adventitious carbon 1s peak at 284.6 eV as a reference. All of the high-resolution spectra were fitted into its components using Gaussian peaks after baseline correction. A Shirley−type background was subtracted from the signals during baseline correction. All the XP spectra were smoothed via the Savitzky−Golay method using a window of 10 points. A survey scan was performed using a pass energy of 200 eV to determine possible contaminants.

2.3.3.2. Energy Dispersive X-Ray Spectroscopy (EDS or EDX)

EDS or EDX is an analytical technique which is used for chemical characterization and elemental analysis of the material under observation. The underlying principle of this technique lies in the interaction of matter with electromagnetic radiation. The distinct atomic structure of each element allows the X-rays which are related to that particular element and is uniquely different from the

other. This analytical technique works jointly with SEM to provide semi-quantitative and qualitative results of the sample [4]. Herein, the EDX pattern and EDX-based elemental mapping images were obtained on the same instrument attached to the scanning electron microscope *i.e.*, "JEOL, JSM Model 6390 LV".

2.3.4. Other Techniques

2.3.4.1. Thermogravimetric Analysis (TGA)

TGA is a thermal analysis where the change in weight of the sample (under observation) is determined as a function of time and temperature. It is a wonderful tool to understand the thermal actions related to nanomaterials. The sample is heated at a fixed heating rate and temperature conditions in a controlled way. The weight change is monitored under programmed conditions. So, TGA can be well utilized to understand thermal events such as adsorption, absorption, desorption, decomposition, sublimation, vaporization, reduction and oxidation. Isothermal mode and scanning mode are the two terms used when the weight changes as a function of time and temperature, respectively [18]. In this work, the TGA data were obtained on a Thermal Analyzer instrument (Model TGA-50, Shimadzu). All the carbon-supported samples were heated up to 700 ^{o}C in an air atmosphere. The heating rate in each case was kept at 10 ^{o}C min^{-1}.

2.3.4.2. N_2 Adsorption/Desorption Analysis

N_2 adsorption/desorption is another method for characterization of the nanomaterials which delivers detailed information about specific surface area, pore size distribution, porous structure and pore volume of the nanomaterials [19]. The working principle is based on the adsorption of a gas on the catalyst surface, N_2 adsorption/desorption isotherms were obtained on a Quantachrome Instrument (model: Nova 1000e) at −196 °C (liquid nitrogen temperature). The specific surface areas of the ECs were determined by the Brunauer−Emmett−Teller (BET) method using the adsorption data at a relative pressure (P/P_0) region of 0.02−0.29. The pore size distribution of the ECs was determined following the Barrett−Joyner−Halenda (BJH) method in the same instrument.

2.4. Electrochemical Characterization

In the current study, the electrochemical characterization of the as-synthesized materials was achieved via cyclic voltammetry (CV), linear sweep voltammetry (LSV) and chronoamperometry (CA), using a rotating disk electrode (RDE) with the help of a standard three-electrode electrochemical cell having a potentiostat/galvanostat (Metrohm Autolab PGSTAT204 workstation, The Netherlands). Ag/AgCl (in saturated KCl) and Pt wire were used as the reference and counter electrodes, respectively. An EC-coated glassy carbon electrode (GCE) with a geometrical surface area of 3 mm diameter was used as the working electrode (WE). The WE was fabricated by preparing a homogeneous suspension of catalyst by ultrasonically mixing the sample materials with distilled water and 2-propanol as solvents and Nafion solution as a binder.

2.4.1. Cyclic Voltammetry (CV)

One of the most prevalent and commonly used electrochemical tools is the CV which measures the potential-current relationship systematically. The CV experiment is carried out in a vessel, known as the electrochemical cell that consists of a standard three-electrode system (Figure 2.2.4). The role of each electrode is described briefly as follows [20]:

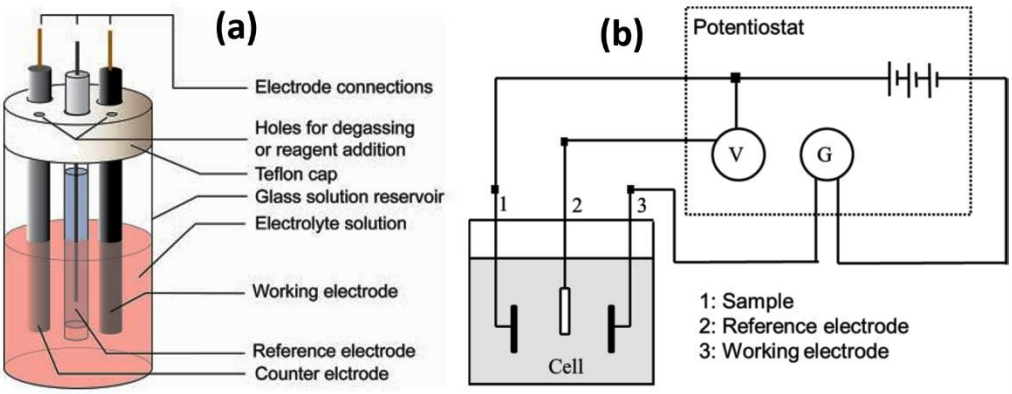

Figure 2.2.4. Schematic representation of a) three-electrode electrochemical system (Adapted from [20]) and b) three-electrode electrical circuit set-up diagram used in electrochemical tests. (Adapted from [21]).

Reference Electrode (RE): It is the electrode having a stable and fixed equilibrium potential, regarding which the potential of other electrodes is measured in the electrochemical apparatus. Thus, the applied potential is usually reported as "vs." a specific reference. The few commonly used reference electrodes include Ag/AgCl electrode, saturated calomel electrode (SCE) and standard hydrogen electrode (SHE).

Working Electrode (WE): It is the electrode where the electrochemical event occurs. The applied potential on the WE is controlled via a potentiostat and is measured with respect to the RE.

Counter electrode (CE): The main role of the CE is to measure the current flows during oxidation or reduction of the analyte as the potential is applied to, WE. The CE completes the electric circuit and measures the current when electrons started flowing between, WE and CE. Typically, Pt wire or disk is used as the CE. However, carbon-based CEs are also used nowadays to a great extent.

The applied potential is varied in both forward and backward directions at a particular scan rate during the current measurement. A backward scan is necessary to bring the electrode potential of the WE to its initial value as CV is a potentiodynamic process. A plot of current vs. applied potential gives the cyclic voltammogram. A cyclic voltammogram gives knowledge about the redox properties (*i.e.*, oxidation and reduction) of a molecular species, qualitative evidence on reaction mechanisms, analysis of electrochemical reaction involving ions and surface atoms of the WE under investigation and so on [22].

2.4.2. Rotating Disk Electrode (RDE)

RDE is a type of hydrodynamic electrode applied in a three-electrode system where 1-D transport occurs [23]. The speed of the RDE can be controlled at various levels. The function of rotation during the evaluation of ORR is to enhance the rate of diffusion of O_2 and electrolyte occurring toward the surface of the electrode. On the other hand, the chief role of rotation is to eliminate the gas bubbles produced during OER from the catalyst surface rapidly. RDE can rotate during the experiments that help flux of analyte towards the electrode. The basic principle of RDE is based

on the rotation of a planar electrode to produce a centrifugal force at the interface of the electrode with a thin layer of solution. Generally, RDE-based experiments use LSV that starts with a potential where there is no Faradaic reaction. Thereafter, the voltage is swept over a range of potential up to around 250 mV beyond redox potential [24]. In LSV, the current at the WE is monitored continuously by changing the potential linearly with time [25].

2.4.3. Chronoamperometry (CA)

CA is a time-dependent electrochemical technique which studies the variation of current as a function of time at a constant potential. The current changes occur at the surface of the WE with respect to the diffusion of layers of the analyte from the bulk solution [26]. In the current study, CA test was carried out to check the stability of the ECs towards the desired reaction in the same electrochemical workstation where CV and LSV experiments were carried out. The CA plots for ORR were obtained in an electrolytic mixture of 0.1 M KOH for 6 h at a constant potential of –0.3 V.

2.4.4. Electrochemical Impedance Spectroscopy (EIS)

EIS measurements were performed to study the kinetics and to identify the resistance of catalyst deposited electrodes performed in 0.1 M KOH solution within the frequency range from 6.2 MHz to 530 Hz. EIS measurements were performed in an electrochemical workstation (SP-300, BioLogic, France) using a 5 MHz polished chromium/gold-coated keyhole quartz resonator (AWS SNS 000026 A, AWSensors, Spain) as the working electrode, a Pt coil as the counter electrode and an Ag/AgCl saturated with KCl solution as the reference electrode.

2.4.5. Electrode Preparation and Electrochemical Activity Towards ORR and OER

The ink was prepared by sonicating 5 mg of the EC in 0.5 mL C_2H_5OH in H_2O (3:2) and 0.5 mL of 0.5 wt.% Nafion solution mixture. After 30 min of sonication, 6 µL of the suspension was drop cast to the polished glassy carbon electrode (GCE) disk to yield a uniform thin film and dried in an inert atmosphere at

35 °C for 12 h (Figure 2.2.5). An aqueous solution of 0.1 M KOH de-aerated with N_2 gas was used as an electrolyte for the CV, and RDE studies. During the electrochemical investigations, the electrolyte was saturated with N_2 to achieve an inert environment and O_2 to achieve an oxygen-rich atmosphere.

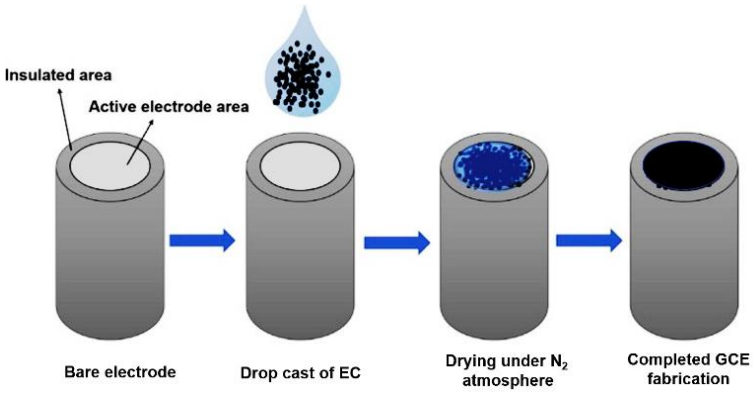

Figure 2.2.5. Diagrammatic representation of the fabrication of EC over GCE.

CV experiments were performed in N_2- and O_2-saturated 0.1 M aqueous solution of KOH in a potential window of 0.2 to –0.8 V (vs. Ag/AgCl). Prior to N_2- and O_2-saturated scans, ultra-high pure N_2 and O_2 were purged for 30 min for making a saturated environment and the flow was also continued during the tests. The working electrode was subjected to a continuous CV cycle between 0.2 to –0.8 V (vs. Ag/AgCl) at a scan rate of 100 mV s^{-1} till a reproducible CV curve was obtained. After surface cleaning, the final CV plot was obtained in O_2-saturated electrolyte at a scan rate of 50 mV s^{-1}. The potentials in a Ag/AgCl and SCE electrode were converted vs. RHE using the relations: $E_{RHE} = E_{Ag/AgCl} + E^{o}_{Ag/AgCl} + 0.059$ pH and $E_{RHE} = E_{SCE} + E^{o}_{SCE} + 0.059$ pH [27,28] where, E_{RHE} is the reversible hydrogen electrode potential, $E_{Ag/AgCl}$ is Ag/AgCl electrode potential and $E^{o}_{Ag/AgCl}$ is standard Ag/AgCl electrode potential = 0.1976 V at 25 °C while E_{SCE} is calomel electrode potential and $E^{o}_{Ag/AgCl}$ is standard calomel electrode potential = 0.244 V at 25 °C and pH of 0.1 M KOH = 13

The same WEs fabricated were then used for RDE measurement that is attached to the same electrochemical analyzer. LSV curves were obtained in the potential range of 0.2 to –0.8 V and 0.2 to 1.5 V (vs. Ag/AgCl) for ORR and OER, respectively at a scan rate of 10 mV s^{-1} in O_2-saturated 0.1 M KOH solution. The

rotation speed applied during OER is 1600 rpm. For determination of the number of electrons transferred (n) during ORR, RDE experiments were carried out at different rotations (400, 900, 1600, 2500 and 3600 rpm) to obtain the Koutecky–Levich (K–L) plots [27]. RDE experiments for both reactions were conducted in an O_2-saturated 0.1 M aqueous solution of KOH. The currents obtained were normalized to the geometric surface area of the GCE for all the samples. For OER, overpotential at 10 mA cm^{-2} (η_{10}) is calculated using the following equations: $E_{experimental} - E_{theoretical}$, where $E_{theoretical}$ = 1.23 V (vs. RHE). Based on the measured ORR LSV polarization curves, the number of electrons (n) involved in a single ORR cycle is evaluated employing Koutecky-Levich (K-L) equation [29]:

$$\frac{1}{j} = \frac{1}{j_k} + \frac{1}{B\,\omega^{0.5}} \quad \frac{1}{j} = \frac{1}{j_k} + \frac{1}{B\,\omega^{0.5}} \tag{2.4}$$

$$B = 0.62\ nF\ (Do_2)^{2/3} \vartheta^{-1/6}\ Co_2 \tag{2.5}$$

where j, j_k and ω are the current density, kinetic current density and the angular rotation rate of the electrode. B is the Levich Constant, F is the Faraday constant (96500 C mol^{-1}), Do_2 is the diffusion coefficient of O_2 in 0.1 M KOH (2.0×10^{-5} cm^2 s^{-1}), ϑ is the kinetic viscosity (0.01 cm^2 s^{-1}) and Co_2 is the bulk concentration of O_2 (1.2×10^{-6} mol cm^{-3}).

The double-layer capacitance (C_{dl}) was determined for the ECs to determine electrochemically active surface area (ECSA). To get C_{dl}, a non-Faradaic potential region with no redox processes taking place must be identified from the CV curve obtained in an N_2-saturated 0.1 M aqueous solution of KOH. The current acquired in the non-Faradaic potential range is the double-layer charging current. Afterwards, scan rate-dependent CVs were obtained in a 0.1 V window around the open-circuit voltage. The current measured in this potential region is due to the double-layer charging. The plot of charging current as a function of scan rate gives a straight line with a slope which is equal to C_{dl}. ECSA is then calculated by dividing C_{dl} by the specific capacitance (C_S) according to the following equation [30]:

$$ECSA = C_{dl} / Cs \tag{2.6}$$

CA test was performed in an O_2-saturated 0.1 M KOH solution at –0.3 V (vs. Ag/AgCl) for 6 h to check the stability of the ECs. During the CA test, the rotation rate of the WE was maintained to be 1600 rpm. The accelerated durability test (ADT) was carried out to determine the durability of the ECs towards ORR up to 10000 CV cycles in O_2-saturated 0.1 M KOH solution and compared with standard 20 wt% Pt/C. This experiment involved LSV measurement at 1600 rpm before and after 10000 potential CV cycles.

References

[1] Cullity, B. D. Elements of X-ray Diffraction. In Cohen, M., consulting editor, *Addison-Wesley metallurgy series, Addison-Wesley Publishing*, 1956.

[2] Klug, H. P., and Alexander, L. E. X-ray diffraction procedures: For polycrystalline and amorphous materials, 2nd Edition. 992, ISBN 0-471-49369-4, Wiley-VCH, 1974.

[3] Mourdikoudis, S., Pallares, R. M., and Thanh, N. T. Characterization techniques for nanoparticles: Comparison and complementarity upon studying nanoparticle properties. *Nanoscale*, 10(27):12871–12934, 2018.

[4] Boddolla, S., and Thodeti, S. A review on characterization techniques of nanomaterials. *International Journal of Engineering, Science and Mathematics*, 7(1):169–175, 2018.

[5] Sivanantham, A., Ganesan, P., and Shanmugam, S. A synergistic effect of Co and CeO_2 in nitrogen-doped carbon nanostructure for the enhanced oxygen electrode activity and stability. *Applied Catalysis B: Environmental*, 237:1148–1159, 2018.

[6] Sudarsanam, P., Hillary, B., Amin, M. H., Rockstroh, N., Bentrup, U., Brückner, A., and Bhargava, S. K. Heterostructured copper-ceria and iron-ceria nanorods: Role of morphology, redox, and acid properties in catalytic diesel soot combustion. *Langmuir*, 34(8):2663−2673, 2018.

[7] Parwaiz, S., Bhunia, K., Das, A. K., Khan, M. M., and Pradhan, D. Cobalt-doped ceria/reduced graphene oxide nanocomposite as an efficient oxygen reduction reaction catalyst and supercapacitor material. *The Journal of Physical Chemistry C*, 121(37):20165–20176, 2017.

[8] Orlando, A., Franceschini, F., Muscas, C., Pidkova, S., Bartoli, M., Rovere, M., and Tagliaferro, A. A comprehensive review on Raman spectroscopy applications. *Chemosensors*, *9*(9):262, 2021.

[9] What is Raman Spectroscopy? *Accessed 12 October 2022 https://www.edinst.com/ko/blog/what-is-raman-spectroscopy/*

[10] Popović, Z. V., Dohčević-Mitrović, Z., Šćepanović, M., Grujić-Brojčin, M., and Aškrabić, S. Raman scattering on nanomaterials and nanostructures. *Annalen der Physik*, 523(1-2):62–74, 2011.

[11] Mohammed, A., and Abdullah, A. Scanning electron microscopy (SEM): A review. In Matache, G., Popescu, A.-M., and Hristea, A., editors, *Proceedings of 2018 International Conference on Hydraulics and Pneumatics-HERVEX*, pages 77–85, ISSN:1454-8003. Băile Govora, Romania Scanning, 7-9 November 2018,

[12] Farré, M., and Barceló, D. Introduction to the analysis and risk of nanomaterials in environmental and food samples. In Farré, M., and Barceló, D., editors, *Comprehensive Analytical Chemistry*, volume 59 of *Analysis and Risk of Nanomaterials in Environmental and Food Samples*, pages 1–32, ISBN: 978-0-444-56328-6. Elsevier, 2012.

[13] Baidya, T., Mazumder, T., Koltunov, K. Y., Likhar, P. R., Clark, A. H., Tiwari, K., Sobolev, V. I., Payra, S., Murayama, T., Lin, M., Bera, P., Roy, S., Biswas, K., Safonova, O., Rao, B. S., and Haruta, M. Low-temperature propylene epoxidation activity of CuO-CeO_2 catalyst with CO + O_2: Role of metal-support interaction on the reducibility and catalytic property of CuO_x species. *The Journal of Physical Chemistry C*, 124(26):14131–14146, 2020

[14] Bêche, E., Charvin, P., Perarnau, D., Abanades, S., and Flamant, G. Ce 3d XPS investigation of cerium oxides and mixed cerium oxide ($Ce_xTi_yO_z$). *Surface and Interface Analysis*, 40(3-4):264–267, 2008.

[15] Briggs, D. Practical surface analysis. Auger and X-Ray Photoelectron Spectroscopy. In Briggs, D., and Seah, M. P., editors, ISBN: 978-0471920816, Wiley, 1990.

[16] Siegbahn, K. Alpha-, beta-and gamma-ray spectroscopy. In Siegbahn, K. editor, Ray Spectroscopy, vol 1, ISBN: 0 444 10695 2, Elsevier, 2012.

[17] Marghany, M. Chapter 3 - Quantization of Maxwell's equations. In Marghany,

M. editor, *Synthetic Aperture Radar Imaging Mechanism for Oil Spills*, pages 41-60, ISBN: 9780128181119, Gulf Professional Publishing, 2020.

[18] Loganathan, S., Valapa, R. B., Mishra, R. K., Pugazhenthi, G., and Thomas, S. Thermogravimetric analysis for characterization of nanomaterials. In Thomas, S., Thomas, R., Zachariah, A. K., and Mishra, R. K., editors, *Thermal and Rheological Measurement Techniques for Nanomaterials Characterization*, volume 3 of *Micro and Nano Technologies*, pages 67–108, ISBN:978-0-323-46139-9. Elsevier, 2017.

[19] Akshatha, S., Sreenivasa, S., Parashuram, L., Udaya, V., Alharthi, F. A. and Rao, T. M. C. Microwave-assisted green synthesis of p-type Co_3O_4@mesoporous carbon spheres for simultaneous degradation of dyes and photocatalytic hydrogen evolution reaction. *Materials Science in Semiconductor Processing*, 121:105432, 2021.

[20] Rountree, K. J., Mccarthy, B. D., Rountree, E. S., Eisenhart, T. T., and Dempsey, J. L. A practical beginner's guide to cyclic voltammetry. *Journal of Chemical Education*, 95:197−206, 2018.

[21] Padrós, R., Giner-Tarrida, L., Herrero-Climent, M., Punset, M., and Gil, F. J. Corrosion resistance and ion release of dental prosthesis of CoCr obtained by CAD-CAM milling, casting and laser sintering. *Metals*, 10(6):827, 2020.

[22] Joshi, P. S. and Sutrave, D. S. A brief study of cyclic voltammetry and electrochemical analysis. *International Journal of ChemTech Research*, 11(9):77−88, 2019.

[23] Masa, J., Batchelor-McAuley, C., Schuhmann, W., and Compton, R. G. Koutecky–Levich analysis applied to nanoparticle modified rotating disk electrodes: Electrocatalysis or misinterpretation, *Nano Research*, 7(1):71−78, 2014.

[24] Sandford, C., Edwards, M. A., Klunder, K. J., Hickey, D. P., Li, M., Barman, K., Sigman, M. S., White, H. S., and Minteer, S. D. A synthetic chemist's guide to electroanalytical tools for studying reaction mechanisms. *Chemical Science*, 10(26):6404−6422, 2019.

[25] Evans, D. H. Review of voltammetric methods for the study of electrode reactions. In Montenegro, M. I., Queirós M. A., and Daschbach J. L., editors,

Microelectrodes: Theory and Applications, volume 197 of *NATO ASI Series (Series E: Applied Sciences)*, pages 17−32, ISBN: 978-94-011-3210-7. Springer-Dordrecht, 1991.

[26] Rezaei, B., and Irannejad, N. Electrochemical detection techniques in biosensor applications. In Ensafi, A. A., editor, *Electrochemical Biosensors*, pages 11–43, ISBN: 978-0-12-816491-4. Elsevier, 2019.

[27] Ahmed, M. S., Choi, B., and Kim, Y. B. Development of highly active bifunctional electrocatalyst using Co_3O_4 on carbon nanotubes for oxygen reduction and oxygen evolution. *Scientific Reports*, 8:2543, 2018.

[28] Magni, M., Postiglione, E., Marzorati, S., Verotta, L., and Trasatti, S. P. Green corrosion inhibitors from agri-food wastes: The case of Punica granatum extract and its constituent ellagic acid. A validation study. *Processes*, 8(3):272, 2020.

[29] Liu, R., Wu, D., Feng, X., and Müllen, K. Nitrogen-doped ordered mesoporous graphitic arrays with high electrocatalytic activity for oxygen reduction. *Angewandte Chemie International Edition*, 49(14):2565-2569, 2010.

[30] McCrory, C. C., Jung, S., Ferrer, I. M., Chatman, S. M., Peters, J. C., and Jaramillo, T. F. Benchmarking hydrogen evolving reaction and oxygen-evolving reaction electrocatalysts for solar water splitting devices. *Journal of the American Chemical Society*, 137(13):4347–4357, 2015.